

<https://doi.org/10.1038/s41528-025-00482-9>

# Rethinking organic electrochemical transistor modeling: the critical role of volumetric capacitance in predictive 2D Nernst-Planck-Poisson simulations



Ihor Sahalianov<sup>1,2,6</sup>✉, Aleksandar Y. Mehandzhiyski<sup>1,3,6</sup>, Peter Andersson Ersman<sup>4</sup> & Igor Zozoulenko<sup>1,3,5</sup>✉

Organic electrochemical transistors (OECTs) combine electron/ionic transport with organic semiconductor flexibility to connect biology and electronics. As they approach industrial use, optimizing performance requires accurate modeling of their structure. This study presents a two-dimensional (2D) OECT model based on Nernst–Planck–Poisson equations that explicitly includes volumetric capacitance ( $C_v$ ). Unlike previous models that ignore  $C_v$ , our model highlights its essential role in OECT operation, allowing us to accurately match the measured output currents of PEDOT:PSS printed OECTs. We studied how parameters like diffusion coefficients of holes and ions, fixed anion concentration, and intrinsic capacitance affect transistor performance. We analyze existing OECT models, noting that different frameworks, despite varying assumptions, can reproduce data. This question relies solely on experimental agreement for validation. We argue that models should also be evaluated on their physical principles. To assist readers, we provide COMSOL.mph files for 1D and 2D OECT models for device design and optimization.

An organic electrochemical transistor (OECT) consists of an organic semiconductor film serving as an active conducting channel interfaced with source and drain electrodes (usually made of metal or carbon) and an electrolyte, with a gate electrode either submerged into or deposited on top of it. The principle of OECT operation relies on ions being injected from the electrolyte to the channel, enabling mixed ionic and electron transport. The ionic motion modulates the electrical current flowing through the channel, making OECTs highly sensitive to biological and chemical changes in their environment<sup>1</sup>.

The OECTs are not designed to match inorganic transistors in terms of high-speed performance. Instead, their advantage lies in being made from organic materials, which impart superior mechanical properties such as flexibility, viscoelasticity and low Young's modulus. OECTs demonstrated stability on different substrates with potential for industrial-scale printing<sup>2,3</sup>. Another advantage is their compatibility with aqueous environments, making them suitable for integration with biological systems such as sweat<sup>4</sup>,

saliva<sup>5</sup>, blood<sup>6,7</sup>, brain tissue<sup>8</sup> and others<sup>9</sup>. The main applications of OECTs stem from two key properties: their scalability in fabrication, which enables low-power chemical sensing solutions<sup>10</sup>, and their excellent stability in both in vivo and in vitro environments, which leads to applications in biology<sup>11</sup>. These include on-site monitoring of cells and tissue<sup>12,13</sup>, as well as biosensors targeting neurotransmitters<sup>14</sup>, metabolites (cholesterol<sup>5</sup>, glucose<sup>15</sup>, lactate<sup>16</sup>) or various pathogens<sup>17,18</sup>.

The active material in an OECT's conductive channel can be a variety of mixed ion-electron conducting organic semiconductors. However, one of the most widely used materials is poly(3,4-ethylenedioxythiophene):polystyrene sulfonate (PEDOT:PSS), known for its excellent mixed ion-electron conductivity. In PEDOT:PSS, holes (polarons) serve as the primary charge carriers, counterbalanced by deprotonated sulfonyl groups from the PSS chains<sup>19</sup>, enabling efficient ion diffusion through water-filled pores (see inset of Fig. 1 for schematic representation) in the material<sup>20</sup>. PEDOT:PSS-based OECTs exhibit high

<sup>1</sup>Laboratory of Organic Electronics, Department of Science and Technology, Linköping University, Norrköping, Sweden. <sup>2</sup>Wallenberg Initiative Materials Science for Sustainability, Department of Science and Technology, Linköping University, Norrköping, Sweden. <sup>3</sup>Model One AB, Norrköping, Sweden. <sup>4</sup>RISE Research Institutes of Sweden, Digital Systems, Smart Hardware, Printed, Bio- and Organic Electronics, Norrköping, Sweden. <sup>5</sup>Wallenberg Wood Science Center, Linköping University, Norrköping, Sweden. <sup>6</sup>These authors contributed equally: Ihor Sahalianov, Aleksandar Y. Mehandzhiyski. ✉e-mail: [ihor.sahalianov@liu.se](mailto:ihor.sahalianov@liu.se); [igor.zozoulenko@liu.se](mailto:igor.zozoulenko@liu.se)

transconductance ( $g^*$ ), a key figure of merit that determines device performance in terms of sensitivity, signal amplification, and ion-electron coupling efficiency<sup>1</sup>. The transconductance is given by  $g^* = \mu C_V$ , where  $\mu$  is the hole mobility and  $C_V$  is the volumetric capacitance, highlighting the crucial role of volumetric capacitance in OECT operation. The capacitance of PEDOT:PSS originates from electrostatic Stern layers formed between holes and counterions throughout the material's volume, with contributions from both classical and quantum effects<sup>21–23</sup>.

Extensive academic research on OECTs indicates that the technology is maturing and transitioning toward industrial-scale applications. At this stage, performance optimization takes center stage. A comprehensive theoretical understanding of OECT operation, combined with full device modeling, is essential for rapidly and cost-effectively predicting optimized geometries and parameters tailored to specific applications.

One of the first models to predict the current-voltage characteristics of OECTs was the Bernards and Malliaras model, which has been instrumental in shaping the theoretical understanding and conceptual framework of these devices by describing them as coupled ionic and electronic circuits<sup>24</sup>. Building on the seminal work of Bernards and Malliaras, numerous studies using the equivalent circuit models have explored various aspects of OECT performance, examining the key factors influencing their operation. For a comprehensive review of different models, see a perspective by Tu and Fabiano<sup>25</sup> and a topical review by Colucci et al.<sup>26</sup>.

The above-mentioned approaches provide valuable insight into the physical behavior of OECTs but are often limited to retrospective analysis, offering a phenomenological explanation of experimentally observed characteristics after electrical characterization has been performed. As a result, their applicability as predictive tools for the output and transfer curves of OECTs remains constrained.

In this context, a numerical approach based on the Nernst–Planck–Poisson (NPP) equations offers a significant advantage, enabling a deeper understanding of the physical and operational phenomena governing OECT performance. By incorporating device geometry and material parameters, the NPP framework provides a more accurate predictive description of experimental behavior. In recent years, the NPP approach has been successfully applied to a range of organic and electrochemical devices, including supercapacitors<sup>22,23,27,28</sup>, electrolyte-gated field-effect transistors<sup>29,30</sup>, electrochemical cells<sup>31,32</sup>, and OECTs.

Several studies have implemented one-dimensional (1D) Nernst–Planck–Poisson (NPP) models to describe the electrical behavior of OECTs (Prigodin et al.<sup>33</sup> Shirinskaya et al.<sup>34</sup> Tybrandt et al.<sup>28</sup> Keene et al.<sup>35</sup>). It is critically important to emphasize that most of these studies—specifically Prigodin et al.<sup>33</sup> Tybrandt et al.<sup>28</sup> and Keene et al.<sup>35</sup>—incorporate the key material parameters of PEDOT:PSS, the volumetric capacitance  $C_V$ , as an essential input parameter in their models, even though these studies differ in how exactly  $C_V$  is incorporated into the NPP equations.

However, the predictive power of 1D models still remains rather limited, as they are not in a position to account for key geometrical features crucial for OECT operation. These include the presence of electrolyte reservoirs separated from the active channel, the spatial arrangement of the gate, source, and drain electrodes, and other structural and geometrical aspects that influence device performance.

To overcome these limitations and enable truly predictive OECT models, two-dimensional (2D) NPP models are necessary. Such models have recently been reported in the literature<sup>36–39</sup>. However, the predictive accuracy of 2D models depends on their ability to correctly capture the fundamental physics governing OECT operation. Do the reported models meet this requirement? Unfortunately, we cannot give a positive answer. The key issue is that, unlike the aforementioned 1D models, which explicitly include volumetric capacitance  $C_V$  as a fundamental input parameter, the above-mentioned 2D models do not incorporate  $C_V$  in their description of OECT operation. In our view, neglecting  $C_V$  in OECT modeling is analogous to omitting conductivity in the description of current flow in a conductor—it overlooks the most essential material parameter required for accurately capturing device behavior. Therefore, a truly predictive 2D NPP

model that accurately describes the underlying physics of OECTs—specifically by incorporating volumetric capacitance—remains absent.

In this study, we extend the 1D Nernst–Planck–Poisson (NPP) model introduced by Tybrandt et al.<sup>28</sup> to a 2D predictive OECT framework that explicitly incorporates volumetric capacitance, thereby coupling the electron and ion phases in the Poisson equation. This distinguishes our approach from previous 2D models. It is worth noting that the 2D model based on the 1D Tybrandt et al.'s<sup>28</sup> approach has been extended into 2D geometry and applied to PEDOT:cellulose-based supercapacitors<sup>22</sup>, including pseudo-3D model (2D revolution) cases<sup>40</sup>, and also used for modeling of potassium delivery in ionic actuators<sup>41</sup>.

We demonstrate that our model achieves perfect agreement with the experimental output currents of PEDOT:PSS-based printed OECTs, capturing all key aspects of device performance. Additionally, our analysis highlights a significant issue: vastly different theoretical models, despite varying physical assumptions and parameter values, can reproduce experimental results. This suggests that model validation should be based not only on data fitting but also on the validity of underlying physical principles. To enhance reproducibility, we provide COMSOL.mph files and a digital twin simulator. Future work will focus on extending the model to capture the transient behavior of OECTs.

## Results

### 1D model

We start with the 1D model and validate its predictions by comparing them with the experimentally measured output currents, recorded for different gate voltages (Fig. 2a). We fitted the diffusion coefficient of holes to achieve the best possible agreement between the output current at  $V_G = 0$  and the experimental data, which was obtained with the  $D_p$  value listed in Table 1. As shown in Fig. 2a, this adjustment enabled the 1D model to accurately reproduce the output currents at  $V_G = 0$ . However, at higher gate voltages, discrepancies between the simulations and experiments accumulated, leading to a progressively poorer agreement as  $V_G$  increased. Notably, the absence of negative charge carriers (counterions) in the 1D model results in a potential profile that remains entirely positive throughout the channel, showing discontinuities at the source/drain electrode to satisfy the boundary conditions.

### 2D model

Contrary to the 1D model, which shows only qualitative agreement with the experiment, our expanded 2D model perfectly reproduces the output and transfer currents for all gate voltages (see Fig. 2d and Fig. S2). A key improvement in the 2D model is the incorporation of ionic effects in the electrolyte phase, which refines the calculation of the electric hole potential  $V_p$  along the channel. As a result, the simulated potential exhibits a gradual decrease from the source to drain, reaching negative values as prescribed by the boundary conditions at the source/drain electrode (Fig. 2e). It is noteworthy, the overall shape of the potential profile remains consistent with that obtained from the 1D model (apart from the above-mentioned discontinuities of 1D potential at the electrodes). Further, both the 1D (Fig. 2c) and 2D (Fig. 2f) simulations show that hole concentrations are highest near the source and gradually decrease toward the drain, in line with expectations. Note that the hole concentration is higher for the 2D model, as it is compensated by the negative counterions and/or fixed charges. Additionally, higher gate voltages induce channel depletion, leading to a reduced hole density  $\rho$ . These findings—namely, the qualitatively similar predictions of the 1D and 2D models—highlight the crucial role of volumetric capacitance in regulating OECT performance. This behavior can be effectively captured even within a simplified 1D framework, where the electrolyte effect is not explicitly included in the equations but instead incorporated through the gate voltage  $V_G$  at the source and drain boundary conditions.

### The choice of parameters

A comment is warranted regarding the choice of parameters in our simulations. The best fit to the experimental data was achieved at

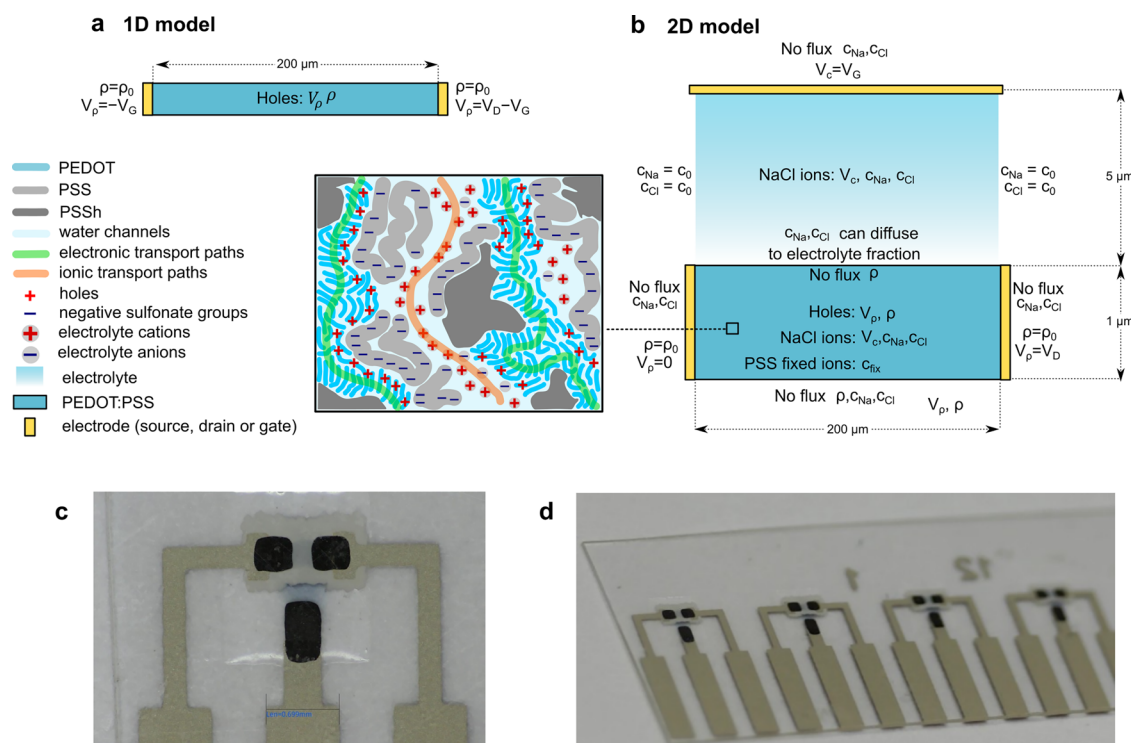


**Fig. 1 | OEFT in experimental studies and simulation models.** Schematic depiction of **a** the 1D and **b** 2D models, including electrodes, electrolyte and channel phases, main variables and boundary conditions. The inset shows the schematic morphology of PEDOT:PSS. **c** A microscope image of one of screen printed OEFTs

evaluated in this study. The image is recorded through the PET substrate, thereby showing also the PEDOT:PSS-based transistor channel and the carbon-based source and drain electrodes. **d** A microscope image of several screen printed OEFTs.

**Table 1 | Parameters, used in simulations**

$D_{p_{max}}$	$2e-1 [cm^2/s]$
1D model, $D_p$	$D_{p_{max}}/2$
2D model, $D_p$	$D_{p_{max}}/18$
$D_{c+}$	$2e-5 [cm^2/s]$
$D_{c-}$	$2e-5 [cm^2/s]$
$T$	300 [K]
$C_v$	$204 [mol/(m^3V)] = 19.7 [F/cm^3]$
$c_{fix}$	0.8 [M]
$w_{channel}$	200 [ $\mu m$ ]
$h_{channel}$	1 [ $\mu m$ ]
$h_{electrolyte}$	5 [ $\mu m$ ]
$A$	200 [ $\mu m^2$ ]
$\epsilon_{channel}$	40
$\epsilon_{electrolyte}$	80
$c_0$	0.1 [M]
$\rho_0$	0.15 [M]

$c_{fix} = 0.8$  M. This value is smaller than  $c_{fix} \approx 2.4$  M, corresponding to the density of immobile sulfonate groups in the fully oxidized PEDOT:PSS<sup>28</sup>. The obtained best fit is consistent with the findings extensively discussed in previous studies that not all regions of the PEDOT:PSS contribute to hole transport. Specifically, a significant fraction of the charge carriers can be confined in the regions of PEDOT:PSS that are not connected to the drain and source electrodes via percolative charge pathways<sup>33,42,43</sup>. Hence, in the present case, it can be interpreted that only one-third of the volume (0.8/2.4) of the active material in the experimental device effectively supports charge carrier transport. Furthermore, the hole density

$\rho = 0.15$  M was chosen to be significantly lower than  $c_{fix}$ . Generally, it is expected to be lower by a factor of approximately  $2.5 \times 3 = 7.5$ . Here, the factor 2.5 represents the ratio of monomer units of PSS to those of PEDOT in PEDOT:PSS<sup>1</sup>. The factor 3 accounts for the fact that at the maximum oxidation level of 33%, one hole is delocalized over three PEDOT monomer units<sup>44</sup>, while each PSS monomer carries a charged sulfonate group. Finally, the hole diffusion coefficient ( $D_p$ ), which is related to mobility via the Einstein relation, can vary between samples depending on the specifics of PEDOT:PSS fabrication. Additionally, for a given sample, it may also be density dependent. Typical values of the experimentally reported diffusion coefficients are  $1 \times 10^{-5} cm^2/s - 2.5 \times 10^{-2} cm^2/s$  (corresponding to the mobilities  $1 \times 10^{-4} cm^2/(Vs) - 1 cm^2/(Vs)$ )<sup>45-48</sup>. In our calculations, from the best fit to the experimentally measured OEFT output currents data, we choose its value  $D_p = 0.011 cm^2/s$  for the 2D model and  $D_p = 0.1 cm^2/s$  for the 1D model, which is consistent with the choice of previous modeling studies (see Table 2).

**Charge carrier concentrations**

2D concentration maps of charge carriers (holes and ions) simulated within the 2D model is shown in Fig. 3. The concentration of holes  $\rho$  gradually decrease from the source towards the drain (as discussed above) with little to no difference in a vertical direction (across the channel), see Fig. 3a. This is in the strong contrast to the case of the electrolyte-gated organic field-effect transistor (EGOFET) where the holes are concentrated along the polymer-electrolyte interface<sup>29,49</sup>. This difference is related to the fact that in the OEFT, unlike in the EGOFET, the electrolyte’s ions can freely penetrate the polymeric film, leading to the homogeneous charge concentration across the channel. The concentration of positive ions  $c_{Na}$  in the electrolyte is close to the bulk value of 0.1 M, as specified by the boundary conditions (Fig. 3b). In the electrolyte, the positive charge of  $Na^+$  ions is counterbalanced by the negative charge of  $Cl^-$  ions (Fig. 3c). However, a small fraction of negative ions ( $<0.005$  M) diffuses into the polymer channel due to the concentration

**Table 2 | Different values of constants (diffusion coefficient of holes, ions in the channel, concentration of fixed PSS<sup>-</sup> anions, volumetric capacitance), which were used in previous studies**

	Volkov et al. <sup>23</sup>	Kaple et al. <sup>39</sup>	Szymanski et al. <sup>36</sup>	Shirinskaya et al. <sup>34</sup>	Mele et al. <sup>40</sup>	Tybrandt et al. <sup>28</sup>	Keene et al. <sup>35</sup>	Skowrons et al. <sup>37</sup>	This paper
$D_p$ , [cm <sup>2</sup> /s]	0.0001	0.0026 0.0065	0.013		Max value 0.205 min value 0.003	Max value 0.205 min value 0.003	0.26e-4	0.0026 0.026	0.011 (2D model); 0.025 (1D model)
$D_{ci}$ , [cm <sup>2</sup> /s]	1e-9	0.26e-5	0.26e-4		3.34e-6 5.08e-6	3.34e-6 5.08e-6	0.26e-4	0.26e-5	0.2e-4
$c_{fix}$ , M	1	0.16	0.33	0.016 0.023	2.4	2.4 ± 0.4	3.5	1.6e-10–1.6	0.8
$C_v$ , [F/cm <sup>3</sup> ]					19.6	19.7	40		19.7

The mobility was converted to a diffusion coefficient according to:  $D = \mu k_B T / e$ . Conversion of the concentration of charge carriers in [cm<sup>-3</sup>] to [M] was obtained via  $c_{inM} = c_{incm-3} * F / e$ , consistent with the relation  $1[M] \approx 6.022e20[cm^{-3}]$ . In PEDOT:PSS, the concentration of  $c_{fix} \approx 2.4 \pm 0.4$  [M] can be related to the oxidation level 33%<sup>28</sup>.

**1D model**

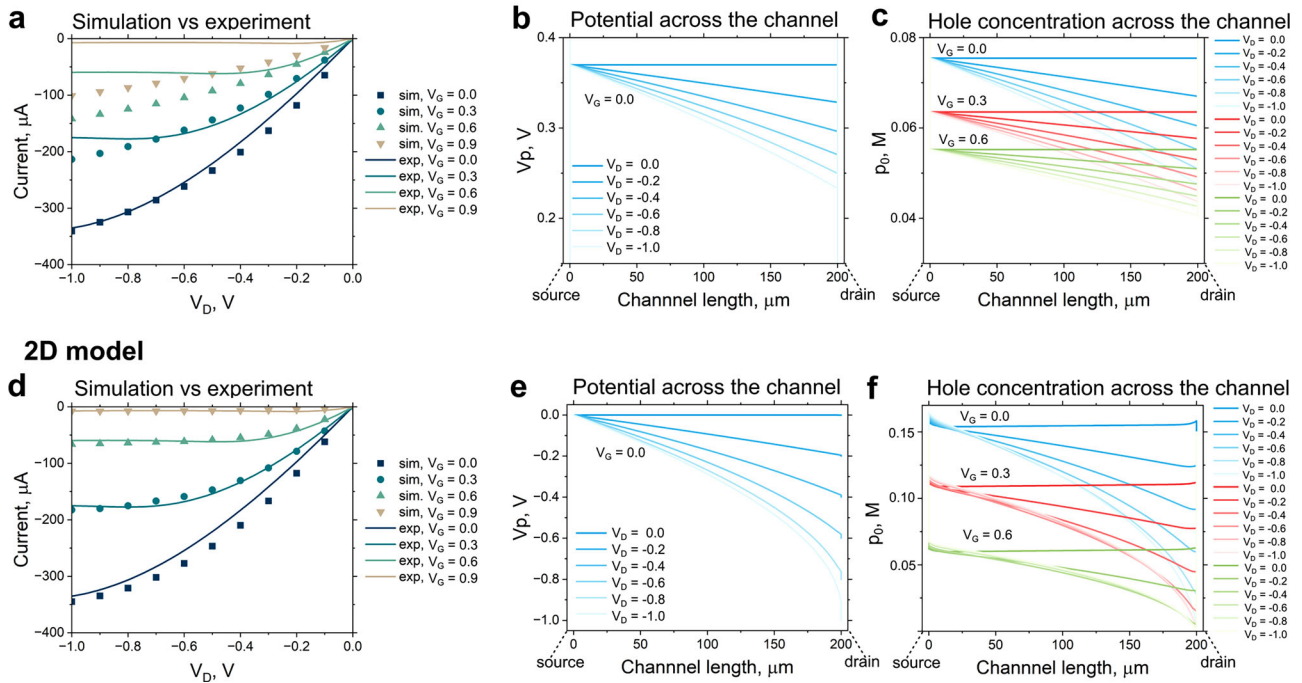


**Fig. 2 | Comparison of the OECT performance, simulated with 1D and 2D models. a, d** Comparison of the OECT output currents measured experimentally and simulated for the 1D and 2D models, respectively. **b, e** Potentials of holes  $V_p$

extracted across the channel at different drain voltages for the 1D and 2D models, respectively. **c, f** Concentration of holes  $\rho$  extracted across the channel at different drain and gate voltages for the 1D and 2D models, respectively.

gradient between mobile anions in the channel and the bulk electrolyte (due to the second term in Eq. 3). Within the channel,  $c_{Na}$  is significantly higher than its bulk values (Fig. 3b), because the Na<sup>+</sup> ions, along with the holes, maintain the overall charge neutrality as shown in Fig. 3d. Charge neutrality is no longer maintained at the polymer-electrolyte interface, where a nanoscale-thick double layer forms. This formation is associated with a sharp gradient in the hole and fixed ion concentrations at the interface. These gradients, in turn, create a positive Na<sup>+</sup> ion concentration gradient. However, some Na<sup>+</sup> ions diffuse into the electrolyte due to the chemical gradient. Notably, Na<sup>+</sup> ions can move freely in both the electrolyte and the polymer channel, whereas holes remain confined to the polymer and do not penetrate the electrolyte.

**The impact of key parameters of the 2D model on OECT performance**

Summarizing the above observations, we conclude that while the simplified 1D model captures the main aspects of OECT performance, the 2D model

significantly improves accuracy and provides simulation results that are in good agreement with the experiments. However, an important question arises: whether the agreement with the experiment is a sufficient criterion for model validation? In several previous studies, such agreement was reported, despite the vastly different theoretical models being used. To explore this, we studied the impact of key parameters of the 2D model on OECT performance, including the hole and ion diffusion coefficients, the fixed charge concentration, and the intrinsic capacitance.

We begin with a key material property: the diffusion coefficient of holes,  $D_p$ . We previously discussed the experimentally reported values of  $D_p$  when justifying our choice of parameters for the simulations. Figure 4a presents the simulated output current at different diffusion coefficients, showing a linear dependence of current on  $D_p$ . This behavior can be understood through the relationship between current density  $j$  and mobility  $\mu$ ,  $j = e\rho\mu$ , where mobility is, in turn, related to the diffusion coefficient via the Einstein relation. It is worth noting that hole mobility can vary significantly between different PEDOT:PSS films, depending on fabrication

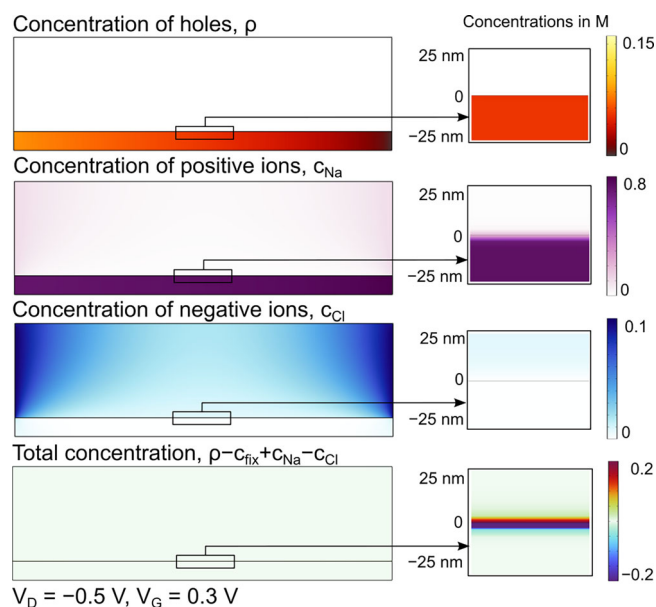


**Fig. 3 | Different charge carrier concentration maps.** a–d Concentration maps of (a) holes, (b) positive and (c) negative ions, and (d) the total charge in the OECT at  $V_D = -0.5$  V,  $V_G = 0.3$  V for the 2D model. The left panel shows the entire device, and the right panel shows the interface between the channel and electrolyte (insets). The length of the channels in the left panel is 20  $\mu$ m.

details. Therefore,  $D_p$  serves as one of the primary fitting parameters in OECT simulations.

The second material property, affecting the output currents, is related to the ionic conductivity of PEDOT:PSS, represented by the diffusivity of ions (both positive and negative),  $D_{ci}$  inside PEDOT:PSS phase. We performed simulations of the output current at different values of  $D_{ci}$  and found that it also strongly affects the results. Higher ionic diffusion coefficients lead to increased output current (Fig. 4b). In previous simulations, a wide range of  $D_{ci}$  values was used, ranging from  $1 \times 10^{-9}$  cm<sup>2</sup>/s to  $0.26 \times 10^{-4}$  cm<sup>2</sup>/s (see Table 2). However, as we argued above when outlining the current understanding of PEDOT:PSS morphology,  $D_{ci}$  should not be treated as a fitting parameter in the model because it is well defined and closely matches the ion diffusion coefficient in water, which is close to  $0.2 \times 10^{-4}$  cm<sup>2</sup>/s.

The third key parameter is  $c_{fix}$ , the concentration of immobile sulfonate groups in the PSS<sup>-</sup> polyelectrolyte within the OECT channel. As mentioned earlier, a typical concentration of  $c_{fix}$  in pristine (as synthesized) PEDOT:PSS is approximately  $c_{fix} \approx 2.4$  M. However, much higher PSS<sup>-</sup> content in PEDOT:PSS films is possible, leading to higher values of  $c_{fix}$ . Conversely, not all regions of the polymer can be available for transport (as argued to be the case for our devices), which results in lower values of  $c_{fix}$ . In previous modeling studies, this parameter was set to different values in a broad range from 0.016 to 3.5 M, as summarized in Table 2. To explore its influence, we simulated output currents at different  $c_{fix}$  and found out, as expected, that higher concentrations lead to higher output currents (Fig. 3c). This behavior can also be understood through the relationship between current density and hole density,  $j = e\rho\mu$ , where a larger  $c_{fix}$  leads to a larger concentration of holes  $\rho$  and subsequently raises the output current. A smaller  $c_{fix}$  enhances the effect of the gate, leading to larger output current drops with increased VG (Fig. S3).

Finally, Fig. 4d illustrates the impact of the volumetric capacitance  $C_V$  on the output currents showing a linear dependence of current on  $C_V$ . Note that most previous models<sup>34,36–39</sup> are not in the position to describe this impact because  $C_V$  was not included in the models.

In conclusion, our findings, presented in Fig. 4, demonstrate that OECT simulation results are highly sensitive to system parameters ( $D_p$ ,  $D_{ci}$ ,  $c_{fix}$ ,  $C_V$ ), opening a wide window of fitting possibilities. This suggests that

different theoretical models, each with distinct sets of fitting—even excluding the intrinsic capacitance as an input parameter—can still be used to reproduce experimental results. As John von Neumann famously stated, “With four parameters I can fit an elephant, and with five I can make him wiggle his trunk,” underscoring the risk of validating a theoretical model solely based on its agreement with experimental data. This overlooks the elephant in the room: the fact that many reported OECT models<sup>34,36–39</sup> do not account for one of the most critical parameters describing the material properties of conducting polymers—the intrinsic capacitance.

## Discussions

In the present paper, based on the 1D Nernst–Planck–Poisson model introduced by Tybrandt et al.<sup>28</sup> we develop a 2D predictive OECT model that accounts for geometrical and structural features of the device and apply it to the analysis of the output characteristics of the printed PEDOT:PSS-based OECTs. The two key features of this model are (i) the use of two sets of equations—one describing hole transport and the other ion transport—each associated with a distinct electrostatic potential,  $V_p$  and  $V_c$ , and (ii) the explicit incorporation of volumetric capacitance  $C_V$ , directly coupling the electron and ion phases in the Poisson equation. This fundamental distinction sets it apart from previous 2D models reported in the literature. Additionally, we consider a minimal 1D model that retains only the most essential factor of the OECT, the volumetric capacitance, and takes gate voltage into account through source and drain boundary conditions.

We demonstrate that the minimal 1D model qualitatively reproduces the experimentally recorded output currents of PEDOT:PSS-based printed OECTs. At the same time, the utilization of the full 2D model allows us to fully capture all aspects of the OECT performance and achieve quantitative agreement with the experiments. The fitted value of the fixed anion concentration (deprotonated sulfonate groups (PSS<sup>-</sup>)) was found to be smaller than that corresponding to the case of fully oxidized PEDOT:PSS. We interpret this as an indication that a significant fraction of the charge carriers is confined in the regions of PEDOT:PSS that are not connected to the drain and source gates via percolative charge pathways, thus not participating in the charge transport.

We also pinpoint that previous OECT models have also reproduced experimental measurements, despite significantly differing in terms of both the physical principles they are built on and the values of the main parameters they used. To address this apparent puzzle, we studied the impact of key parameters of the 2D model on OECT performance, including hole and ion diffusion coefficients, fixed charge concentration, and intrinsic capacitance. We find that the simulation results for the output currents are highly sensitive to system parameters ( $D_p$ ,  $D_{ci}$ ,  $c_{fix}$ ,  $C_V$ ), opening a wide window of fitting possibilities. This suggests that different theoretical models, each with distinct sets of fitting parameters—even excluding the intrinsic capacitance as an input parameter—can still be used to reproduce experimental results. We therefore arrive at the rather unexpected conclusion that an agreement of simulations with the experiment cannot be taken as proof of validation of the utilized model. We argue that the model’s applicability should also be evaluated by the physical principles on which they are built.

We believe that there are still open questions concerning the refinement of the 2D NPP physical models, and more work needs to be done in order to develop a reliable predictive model of the OECT. The central question is how the volumetric capacitance is accounted for in the NPP equations. In the present approach (as well as in ref. 33), this has been done by introducing two separate phases with different potentials, ionic and electronic, coupled through volumetric capacitance. This way of incorporating the volumetric capacitance is motivated by the current understanding of its microscopic origin due to electrostatic Stern layers between holes and counterions, formed throughout the entire volume of a conducting polymer<sup>21–23</sup>. Because the mean-field NPP approach does not resolve the spatial arrangement of holes and ions in the material, introducing the two electrostatic potentials represents a way to account for the Stern layers formed in the volume. In contrast, Keene et al.<sup>35</sup> retained only one common electrostatic potential while introducing the volumetric capacitance through

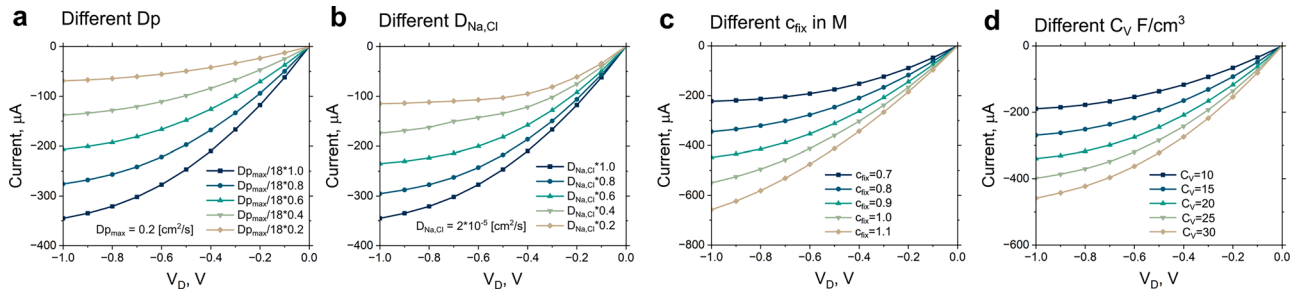


**Fig. 4 | The impact of key parameters on OECT performance.** Dependence of output currents vs. different values of **a** the hole diffusion coefficient, **b** the ion diffusion coefficient, **c** the concentration of PSS<sup>−</sup> anions, and **d** the volumetric capacitance  $C_V$ ;  $V_G = 0$  V.

the gradients of the chemical potential that is related to  $C_V$  via the generalized Einstein relation in the definition of the diffusion current. Further studies are needed to clarify the difference between these models and to determine whether a one-phase model (i.e., without two different potentials for ionic and electronic phases) can adequately describe the operation of devices based on mixed ion-electron conducting polymers.

To ensure that our model is fully reproducible and to allow proficient users to utilize our model we attach the COMSOL .mph files for both 1D and 2D models as parts of the Supporting Information. Alternatively, a standalone simulator (digital twin of the OECT), which does not require any simulation skills or proficiency in COMSOL, will be available at [https://www.model-one.com/].

Finally, while this study focused on the stationary electric characteristics of OECTs, we recognize the importance of dynamic behavior for applications such as signal amplification and neuromorphic systems. Developing time-dependent 2D OECT models based on the same physical principles is a major ongoing effort in our group and will be the focus of a forthcoming, dedicated publication.

## Methods

### Experimental methods

The layout of the OECT screen printing tools was designed using the Clewin software (WieWeb Software Inc., Netherlands). The screen printing processes were carried out in ambient conditions, and all materials were deposited via screen printing onto a flexible 125 µm thick polyethylene terephthalate (PET) plastic substrate by using a flatbed sheet-to-sheet screen printing equipment (DEK Horizon 03iX). The screen printing tools were relying on standard polyester meshes. A different print order may be used to process the OECTs, but the following sequence of the deposited layers was used herein: A silver ink (Ag 5000 purchased from DuPont) was firstly screen printed on top of the flexible PET substrate, to create the contact pads used to probe the source, drain and gate electrodes. This was followed by the screen printing of a PEDOT:PSS stripe serving as the electrochemically active transistor channel (Clevios SV4 purchased from Heraeus), whose edges were located in close proximity to the previously deposited silver layer. Carbon electrodes (7102 conducting screen printing paste purchased from DuPont) were screen printed as the source and drain electrodes in the next processing step, to bridge the gap between the silver layer and the ends of the already deposited PEDOT:PSS-based channel. Each one of the screen-printed layers of silver, PEDOT:PSS and carbon was thermally treated by using a conveyor belt oven (120 °C for 5 min). Subsequently, a pattern of an insulating material (5018 purchased from DuPont) was deposited via screen printing and cured by UV light. Thereafter, an electrolyte ink based on poly(diallyldimethylammonium chloride) dissolved in water (VV009 provided by RISE) was screen printed into the openings of the insulating layer, such that the electrolyte was brought in contact with the PEDOT:PSS-based channel. The deposited electrolyte was transformed into a solid electrolyte layer via UV-curing. The OECT device was then finalized by screen printing a PEDOT:PSS layer on top of

the electrolyte layer, thereby forming the gate electrode. Figure 1c, d shows microscope images of the screen-printed OECTs.

The OECTs evaluated in this study were not encapsulated with adequate barrier films; hence, the OECTs are sensitive to fluctuating environmental conditions. Therefore, all OECT samples were stored and measured in a controlled environment at 20 °C and 50% relative humidity (RH), to enhance the reproducibility. Transfer (drain current vs. gate voltage, at constant drain voltage) and output (drain current vs. drain voltage, for a few different gate voltages) measurements were performed using a semiconductor parameter analyzer (HP/Agilent 4155B) and a function generator (Agilent 33120 A).

### Theoretical methods

OECT simulations were performed within the Nernst–Planck–Poisson model. Equations were solved with the finite element method, implemented in COMSOL Multiphysics 6.3<sup>50</sup>. We consider 1D and 2D models, as schematically depicted in Fig. 1a, b. The 1D model represents the simplest possible OECT model incorporating the volumetric capacitance of PEDOT:PSS. This simplified model includes only holes as charge carriers while explicitly neglecting ions—both those from the electrolyte and PSS<sup>−</sup> fixed ions. Our motivation for studying such a simplistic model is to identify and understand the role of volumetric capacitance in the OECT performance. In contrast, the 2D model includes all relevant ionic species present in the system and accounts for the device geometry, hence providing a full system description. The primary objective of this expanded model is to achieve quantitative agreement with experimental results and, consequently, to serve as a predictive tool for device optimization.

The 2D model includes two sets of equations for holes and ions respectively, represented by their concentrations  $\rho$ , and  $c_{Na}$ ,  $c_{Cl}$  (the latter two collectively referred to as  $c_i$ ) and potentials of the electronic  $V_p$  and ionic phases  $V_c$ .

$$\frac{d\rho}{dt} - \nabla \cdot (D_p (\nabla \rho + f\rho \nabla V_p)) = 0 \quad (1)$$

$$-\frac{\epsilon \nabla^2 V_p}{e} = \rho - (V_p - V_c) C_V \quad (2)$$

$$\frac{dc_i}{dt} - \nabla \cdot (D_{c_i} (\nabla c_i + z_i f c_i \nabla V_c)) = 0 \quad (3)$$

$$-\frac{\epsilon \nabla^2 V_c}{e} = \rho + c_{Na} - c_{Cl} - c_{fix} \quad (4)$$

where  $D_p$  is the diffusion coefficient of holes,  $f = F/RT$ ,  $\epsilon$  is dielectric permittivity,  $e$  is the elementary charge,  $D_{c_i}$  are diffusion coefficients of positive and negative ions,  $z_i$  are ionic charges ( $\pm 1$  in  $e$  units), and  $c_{fix}$  is the concentrations of fixed PSS<sup>−</sup> anions. The two key features of this model, first introduced by Tybrandt et al. in Ref. 28, are: (i) the utilizations of two sets of equations—one for holes and one for ions—with two distinct electrostatic

potentials  $V_p$  and  $V_s$ ; and (ii) the explicit incorporation of volumetric capacitance  $C_V$ , which directly couples the electronic and ionic phases in the Poisson Eq. (2). This fundamental distinction sets it apart from previous 2D models reported in the literature.

Note that immobilized cations, which are present in the solid-state electrolytes, are excluded from the model as they do not contribute to charge transport or directly affect channel behavior, leading to a negligible impact on the OECT output. This simplification also makes the model applicable to a broader range of electrolytes, including aqueous systems. Representation of different electrolytes within our model can be done by a simple change of diffusion coefficients of the electrolyte ions, which will also affect their diffusion in the OECT channel. For clarity, we emphasize that our model accounts for both anionic and cationic species in the electrolyte and the channel, holes in the channel, as well as the immobile PSS anions present in the channel.

It should also be emphasized that the OECT model introduced above, along with the choice of key system parameters, is based on the current understanding of PEDOT:PSS morphology and the origin of volumetric capacitance. Specifically, PEDOT:PSS immersed in water (or an electrolyte) forms a three-phase system consisting of PEDOT-rich regions, PSS-rich regions, and water channels (see Fig. 1)<sup>20,51</sup>. The PEDOT-rich regions contain positively charged PEDOT chains (providing hole transport pathways) balanced by deprotonated PSS<sup>-</sup> chains, while the PSS-rich regions consist of PSS<sup>-</sup> chains compensated by H<sup>+</sup> or Na<sup>+</sup> ions. Ion diffusion in PEDOT:PSS occurs within the water channels, meaning that the ion diffusion coefficients are set close to those in water<sup>52,53</sup> and should not be treated as fitting parameters in the model. Regarding the volumetric capacitance, it originates from microscopic double layers within the film in PEDOT-rich regions, composed of positive charges stored in PEDOT chains that are balanced by negative counterions and/or fixed PSS<sup>-</sup> charges<sup>21,22,54</sup>. The reported volumetric capacitance of PEDOT:PSS falls within the range of 30–300 F cm<sup>-3</sup> [see e.g. ref. 21 and references therein].

The 2D model allows us to directly include gate, source, and drain electrodes in the simulations (Fig. 1b). Boundary conditions for source and drain electrodes were defined on the left and right sides of the channel phase as  $V_p = 0$ , and  $V_p = V_D$ . The gate electrode was placed on top of the electrolyte phase as  $V_c = V_G$ . All other boundary conditions for potentials were set to “zero charge” boundary condition  $n \cdot \nabla D = 0$ . Hole concentration was fixed on the sides of the channel as  $\rho = \rho_0$  and set to “no flux”  $n \cdot (D_i \nabla \rho) = 0$  on the top and bottom of the channel phase. Ionic concentration was set to  $c_i = c_0$  on the sides of the electrolyte phase. On all other boundaries, the “no flux” boundary condition for the ionic phase was set to  $n \cdot (D_i \nabla c_i) = 0$ . Both “no flux” and “zero charge” boundary conditions are default boundary conditions in COMSOL for models that include transport of diluted species and electrostatics.

The 1D model considers only holes as charge carriers, characterized by their concentration ( $\rho$ ) and potential ( $V_p$ ). Unlike the 2D model, which explicitly includes the ionic phase, the 1D model is simplified by excluding it. As a result, the model solely consists of equations governing hole transport,

$$\frac{d\rho}{dt} - \nabla \cdot \left( D_p \left( \nabla \rho + f \rho \nabla V_p \right) \right) = 0 \quad (5)$$

$$-\frac{\varepsilon \nabla^2 V_p}{e} = \rho - V_p C_V \quad (6)$$

The effect of the gate electrode is included in the boundary conditions on the left and right sides of the channel phase as  $V_p = -V_G$  (source electrode), and  $V_p = -V_G + V_D$  (drain electrode). Similarly to the 2D model, the hole concentration was fixed as  $\rho = \rho_0$  on both sides of the channel.

The values of all constants for both 1D and 2D models are listed in Table 2. Boundary conditions and information about systems geometry can be found in Fig. 1. A detailed description of the meshing is provided in the Supporting Information (Figure S1).

To ensure that our model is fully reproducible, we attach the COMSOL.mph files for both 1D and 2D models as parts of the Supporting Information, allowing proficient users to run them using COMSOL. Alternatively, a stand-alone simulator (digital twin of the OECT) will be available at [<https://www.model-one.com/>]. The model is computationally efficient and does not require access to high-performance computational clusters. Simulations were performed on a standard workstation based on the Intel(R) Core(TM) i9-12900K, 3200 MHz, 16 cores (24 Logical processors) and 64 GB RAM. The 1D model produces results almost instantly, with several seconds required to complete. The 2D model is more computationally demanding as it involves computing an initial solution followed by sequential simulations of output curves at various values of  $V_D$  and  $V_G$ . Each subsequent simulation uses the previous solution as the initial guess to aid convergence. For example, for  $V_G = 0.3$  V, the solution obtained for  $V_D = -0.4$  V was used as the initial solution for the system at  $V_D = -0.5$  V. The 2D model, attached as an SI file, requires 8 minutes to compute the initial solution (at  $V_G = 0.0$  and  $V_D = 0.0$ ) and about 19 minutes to simulate 30 points of the output current (for every  $V_G = 0.0, 0.3, 0.6$ , and ten steps of  $V_D$  from  $-0.1$  to  $-1.0$  with the step of  $-0.1$  V).

## Data availability

The data that support the findings of this study are available from the corresponding author upon reasonable request.

Received: 19 June 2025; Accepted: 5 September 2025;

Published online: 23 September 2025

## References

- Rivnay, J., Inal, S., Salleo, A., Berggren, M. & Malliaras, G. G. Organic electrochemical transistors. *Nat. Rev. Mater.* **3**, 17086 (2018).
- Ersman, P. A. et al. All-printed large-scale integrated circuits based on organic electrochemical transistors. *Nat. Commun.* **10**, 5053 (2019).
- Huang, L. et al. Organic electrochemical transistors: from lithography to large-scale printing. *Adv. Electron. Mater.* **11**, 2400474 (2024).
- Currano, L. J., Sage, F. C., Hagedorn, M., Hamilton, L. & Patrone, J. Wearable sensor system for detection of lactate in sweat. *Sci. Rep.* **8**, 15890 (2018).
- Liao, C., Mak, C., Zhang, M., Chan, H. L. W. & Yan, F. Flexible organic electrochemical transistors for highly selective enzyme biosensors and used for saliva testing. *Adv. Mater.* **27**, 676–681 (2015).
- Liu, H. et al. Organic electrochemical transistors for biomarker detections. *Adv. Sci.* **11**, 2305347 (2024).
- Meng, X. et al. Selective ion sensing organic electrochemical transistors suitable for blood analysis. *Adv. Sens. Res.* **3**, 2300097 (2024).
- Feng, J. et al. All-polymer fiber organic electrochemical transistor for chronic chemical detection in the brain. *Adv. Funct. Mater.* **33**, 2214945 (2023).
- Lee, M. Y., Lee, H. R., Park, C. H., Han, S. G. & Oh, J. H. Organic transistor-based chemical sensors for wearable bioelectronics. *Acc. Chem. Res.* **51**, 2829–2838 (2018).
- Yang, C. et al. Low-power/high-gain flexible complementary circuits based on printed organic electrochemical transistors. *Adv. Electron. Mater.* **8**, 2100907 (2022).
- Bai, L., Elósegui, C. G., Li, W., Yu, P. & Fei, J. Biological applications of organic electrochemical transistors: electrochemical biosensors and electrophysiology recording. *Front. Chem.* **7**, 313 (2019).
- Ramuz, M., Hama, A., Rivnay, J., Leleux, P. & Owens, R. M. Monitoring of cell layer coverage and differentiation with the organic electrochemical transistor. *J. Mater. Chem. B* **3**, 5971 (2015).
- Romeo, A. et al. Drug-induced cellular death dynamics monitored by a highly sensitive organic electrochemical system. *Biosens. Bioelectron.* **68**, 791–797 (2015).

14. Tang, H., Lin, P., Chan, H. L. W. & Yan, F. Biosensors and bioelectronics highly sensitive dopamine biosensors based on organic electrochemical transistors. *Biosens. Bioelectron.* **26**, 4559–4563 (2011).
15. Koklu, A. et al. Sensors and actuators: B. chemical Microfluidics integrated n-type organic electrochemical transistor for metabolite sensing. *Sens. Actuators B. Chem.* **329**, 129251 (2021).
16. Gualandi, I. et al. Layered double hydroxide-modified organic electrochemical transistor for glucose and lactate biosensing. *Sensors* **20**, 3453 (2020).
17. Vizzini, P. et al. Detection of *Listeria monocytogenes* in foods with a textile organic electrochemical transistor biosensor. *Appl. Microbiol. Biotechnol.* **107**, 3789–3800 (2023).
18. Löffler, S., Libberton, B. & Richter-dahlfors, A. Organic bioelectronics in infection. *J. Mater. Chem. B* **3**, 4979–4992 (2015).
19. Liang, Y., Offenhäusser, A., Ingebrandt, S. & Mayer, D. PEDOT: PSS-based bioelectronic devices for recording and modulation of electrophysiological and biochemical cell signals. *Adv. Healthc. Mater.* **10**, 2100061 (2021).
20. Sedghamiz, T., Mehandzhiyski, A. Y., Modarresi, M., Linares, M. & Zozoulenko, I. What can we learn about PEDOT: PSS morphology from molecular dynamics simulations of ionic diffusion? *Chem. Mater.* **35**, 5512–5523 (2023).
21. Sahalianov, I., Singh, S. K., Tybrandt, K., Berggren, M. & Zozoulenko, I. The intrinsic volumetric capacitance of conducting polymers: Pseudo-capacitors or double-layer supercapacitors? *RSC Adv.* **9**, 42498–42508 (2019).
22. Sahalianov, I. et al. Volumetric double-layer charge storage in composites based on conducting polymer PEDOT and cellulose. *ACS Appl. Energy Mater.* **4**, 8629–8640 (2021).
23. Volkov, A. V. et al. Understanding the capacitance of PEDOT:PSS. *Adv. Funct. Mater.* **27**, 1700329 (2017).
24. Bernards, D. A. & Malliaras, G. G. Steady-state and transient behavior of organic electrochemical transistors. *Adv. Funct. Mater.* **17**, 3538–3544 (2007).
25. Tu, D. & Fabiano, S. Mixed ion-electron transport in organic electrochemical transistors. *Appl. Phys. Lett.* **117**, 080501 (2020).
26. Colucci, R., de Barbosa, H. F. P., Günther, F., Cavassin, P. & Faria, G. C. Recent advances in modeling organic electrochemical transistors. *Flex. Print. Electron.* **5**, 013001 (2020).
27. Wang, H., Thiele, A. & Pilon, L. Simulations of cyclic voltammetry for electric double layers in asymmetric electrolytes: a generalized modified Poisson–Nernst–Planck model. *J. Phys. Chem. C* **117**, 18286–18297 (2013).
28. Tybrandt, K., Zozoulenko, I. V. & Berggren, M. Chemical potential–electric double layer coupling in conjugated polymer–polyelectrolyte blends. *Sci. Adv.* **3**, 1–7 (2018).
29. Delavari, N., Tybrandt, K. & Berggren, M. Nernst–Planck–Poisson analysis of electrolyte-gated organic field-effect. *J. Phys. D. Appl. Phys.* **54**, 415101 (2021).
30. Popescu, D., Popescu, B., Brandlein, M., Melzer, K. & Lugii, P. Modeling of electrolyte-gated organic thin-film transistors for sensing applications. *IEEE Trans. Electron Devices* **62**, 4206–4212 (2015).
31. Mehandzhiyski, A. Y., Gryszel, M., Gueskine, V. & Zozoulenko, I. Digital twin of a standard electrochemical cell for cyclic voltammetry based on Nernst–Planck–Poisson model. *ACS Electrochem.* **1**, 175–185 (2025).
32. Levey, K. J., Edwards, M. A., White, H. S. & Macpherson, J. V. Simulation of the cyclic voltammetric response of an outer-sphere redox species with inclusion of electrical double layer structure and ohmic potential drop. *Phys. Chem. Chem. Phys.* **25**, 7832–7846 (2023).
33. Prigodin, V. N., Hsu, F. C., Park, J. H., Waldmann, O. & Epstein, A. J. Electron-ion interaction in doped conducting polymers. *Phys. Rev. B - Condens. Matter Mater. Phys.* **78**, 1–9 (2008).
34. Shirinskaya, A., Horowitz, G., Rivnay, J. & Malliaras, G. G. Numerical modeling of an organic electrochemical transistor. *Biosensors* **8**, 103 (2018).
35. Keene, S. T., Rao, A. & Malliaras, G. G. The relationship between ionic-electronic coupling and transport in organic mixed conductors. *Sci. Adv.* **9**, 1–11 (2023).
36. Szymanski, M. Z., Tu, D. & Forchheimer, R. 2-D drift-diffusion simulation of organic electrochemical transistors. *IEEE Trans. Electron Devices* **64**, 5114–5120 (2017).
37. Skowrons, M., Dahal, D., Paudel, P. R. & Lüssem, B. Depletion type organic electrochemical transistors and the gradual channel approximation. *Adv. Funct. Mater.* **34**, 2303324 (2023).
38. Paudel, P. R., Skowrons, M., Dahal, D., Kishen, R. & Krishnan, R. The transient response of organic electrochemical transistors. *Adv. Theor. Simul.* **2100563**, 1–15 (2022).
39. Kaphle, V. et al. Finding the equilibrium of organic electrochemical transistors. *Nat. Commun.* **11**, 2515 (2020).
40. Mele, L. J., Verardo, C. & Palestri, P. Electrochemistry communications reproducing capacitive cyclic voltammetric curves by simulation: when are simplified geometries appropriate? *Electrochem. commun.* **142**, 107378 (2022).
41. Verardo, C., Mele, L. J., Selmi, L. & Palestri, P. Finite-element modeling of neuromodulation via controlled delivery of potassium ions using conductive polymer-coated microelectrodes. *J. Neural Eng.* **21**, ad2581 (2024).
42. Kim, G. & Pipe, K. P. Thermoelectric model to characterize carrier transport in organic semiconductors. *Phys. Rev. B* **8**, 085208 (2012).
43. Ihnatsenka, S., Crispin, X. & Zozoulenko, I. V. Understanding hopping transport and thermoelectric properties of conducting polymers. *Phys. Rev. B* **035201**, 1–12 (2015).
44. Kim, D. & Zozoulenko, I. Why is pristine PEDOT oxidized to 33%? A density functional theory study of oxidative polymerization mechanism. *J. Phys. Chem. B* **123**, 5160–5167 (2019).
45. Zahabi, N. & Zozoulenko, I. Band versus hopping transport in conducting polymers by ab initio molecular dynamics: exploring the effect of electric field, trapping and temperature. *Adv. Electron. Mater.* **2400239**, 1–11 (2024).
46. Fratini, S., Nikolka, M., Salleo, A., Schweicher, G. & Siringhaus, H. Charge transport in high-mobility conjugated polymers and molecular semiconductors. *Nat. Mater.* **19**, 491–502 (2020).
47. Rudd, S. et al. Charge transport and structure in semimetallic polymers. *J. Polym. Sci. Part B Polym. Phys.* **56**, 97–104 (2018).
48. Chauhan, A. K. et al. Enhancement of the carrier mobility of conducting polymers by formation of their graphene composites. *RSC Adv.* **7**, 11913–11920 (2017).
49. Chennit, K. et al. Inkjet-printed, coplanar electrolyte-gated organic field-effect transistors on flexible substrates: fabrication, modeling, and applications in biodetection. *Adv. Mater. Technol.* **8**, 2200300 (2023).
50. COMSOL Multiphysics® v. 6.3. COMSOL AB: Stockholm, Sweden, [www.comsol.com](http://www.comsol.com) (2025).
51. Modarresi, M., Mehandzhiyski, A., Fahlman, M., Tybrandt, K. & Zozoulenko, I. Microscopic understanding of the granular structure and the swelling of PEDOT:PSS. *Macromolecules* **53**, 6267–6278 (2020).
52. Stavrinidou, E. et al. Direct measurement of ion mobility in a conducting polymer. *Adv. Mater.* **25**, 4488–4493 (2013).
53. Lyu, D. et al. Operando NMR electrochemical gating studies of ion dynamics in PEDOT: PSS. *Nat. Mater.* **22**, 746–753 (2023).
54. Proctor, C. M., Rivnay, J. & Malliaras, G. G. Understanding volumetric capacitance in conducting polymers. *J. Polym. Sci. Part B Polym. Phys.* **54**, 1433–1436 (2016).

## Acknowledgements

I.Z. and A.Y.M. acknowledge support from Advanced Functional Materials at Linköping University. I.Z. acknowledges support from Swedish research

Council (2024-04449), and from the Knut and Alice Wallenberg Foundation (KAW) through the Wallenberg Wood Science Center 3.0 (KAW 2021.0313). The computations were performed on resources provided by the National Academic Infrastructure for Supercomputing in Sweden (NAISS) at NSC and PDC.

### Author contributions

I.S. performed simulations and wrote the initial draft of the manuscript. A.M. performed simulations. P.E. provided experimental data. I.Z. conceived and supervised the research. All authors contributed to writing and discussing the manuscript.

### Funding

Open access funding provided by Linköping University.

### Competing interests

The authors, A.M. and I.Z., are shareholders in Model One AB, a company that is interested in exploiting the results reported in this paper.

### Additional information

**Supplementary information** The online version contains supplementary material available at <https://doi.org/10.1038/s41528-025-00482-9>.

**Correspondence** and requests for materials should be addressed to Ihor Sahalianov or Igor Zozoulenko.

**Reprints and permissions information** is available at <http://www.nature.com/reprints>

**Publisher's note** Springer Nature remains neutral with regard to jurisdictional claims in published maps and institutional affiliations.

**Open Access** This article is licensed under a Creative Commons Attribution 4.0 International License, which permits use, sharing, adaptation, distribution and reproduction in any medium or format, as long as you give appropriate credit to the original author(s) and the source, provide a link to the Creative Commons licence, and indicate if changes were made. The images or other third party material in this article are included in the article's Creative Commons licence, unless indicated otherwise in a credit line to the material. If material is not included in the article's Creative Commons licence and your intended use is not permitted by statutory regulation or exceeds the permitted use, you will need to obtain permission directly from the copyright holder. To view a copy of this licence, visit <http://creativecommons.org/licenses/by/4.0/>.

© The Author(s) 2025